Topographic Measurement of Individual Laser Tracks in Alloy 625 Bare Plates

Richard E. Ricker[1] · Jarred C. Heigel[2,3] · Brandon M. Lane[2] · Ivan Zhirnov[4] · Lyle E. Levine[1]

Abstract

Additive manufacturing (AM) combines all of the complexities of materials processing and manufacturing into a single process. The digital revolution made this combination possible, but the commercial viability of these technologies for critical parts may depend on digital process simulations to guide process development, product design, and part qualification. For laser powder bed fusion, one must be able to model the behavior of a melt pool produced by a laser moving at a constant velocity over a smooth bare metal surface before taking on the additional complexities of this process. To provide data on this behavior for model evaluations, samples of a single-phase nickel-based alloy were polished smooth and exposed to a laser beam at three different power and speed settings in the National Institute of Standards and Technology Additive Manufacturing Metrology Testbed and a commercial AM machine. The solidified track remaining in the metal surface after the passing of the laser is a physical record of the position of the air–liquid–solid interface of the melt pool trailing behind the laser. The surface topography of these tracks was measured and quantified using confocal laser scanning microscopy for use as benchmarks in AM model development and validation. These measurements are part of the Additive Manufacturing Benchmark Test Series.

✉ Richard E. Ricker
richard.ricker@nist.gov
http://www.nist.gov/people/richard-e-ricker

Jarred C. Heigel
jarred.heigel@thirdwavesys.com

Brandon M. Lane
brandon.lane@nist.gov

Ivan Zhirnov
ivan.zhirnov@nist.gov

Lyle E. Levine
lyle.levine@nist.gov

1. Materials Measurement Laboratory, National Institute of Standards and Technology, Gaithersburg, MD 20899, USA

2. Engineering Laboratory, National Institute of Standards and Technology, Gaithersburg, MD 20899, USA

3. Present Address: Third Wave Systems, Minneapolis, MN 55344, USA

4. Physical Measurement Laboratory, National Institute of Standards and Technology, Gaithersburg, MD 20899, USA

Introduction

Additive manufacturing (AM) covers a wide range of processes that use digital technologies to manufacture objects by incrementally adding material. While AM covers a diverse range of materials and processes, they all require some form of materials processing to bond the increments of material to the part as it is built. Since the complex design and manufacturing goals of AM benefit from the use of small increments of material, the material processed in the creation of these bonds usually determines the "as-built" properties and post-build processing is usually employed to improve properties. For AM of metallic parts, post-build heat treatments, including hot isostatic pressing (HIPing), are used for this purpose. The microstructures produced by AM processing differ significantly from that of either cast or wrought processing of the same alloy, and it has been shown that this causes them to respond differently to heat treatments [1–10]. Therefore, understanding the final properties in metal AM parts requires understanding how AM processing conditions determine the as-built microstructures

of alloys; and then, how these microstructures respond to post-build heat treatments [1–10].

In traditional subtractive manufacturing, the shape of a part is determined by processes that remove material without altering the microstructure and properties of the remaining material. While there are traditional manufacturing methods that alter microstructures and properties, avoiding these for critical applications enables designers, and approving officials, to utilize tabulated alloy property data for their decision making. To compete with traditional manufacturing methods, AM needs to be able to provide a similar level of certainty for final properties. Computer modeling and simulation is a promising technology for addressing the complex array of variables that determine the "as-built" AM microstructure; and therefore, the microstructure following post-build heat treatments and final properties. The objective of this work is to provide a set of well characterized benchmarks to aid in the development of these models. Specifically, these benchmark measurements are part of a comprehensive set of in-situ and ex-situ measurements of single laser traces, designated AMB2018-02 within the 2018 Additive Manufacturing Benchmark Test Series (AM-Bench). Further information about these laser trace benchmarks may be found in the references [11–13].

Laser powder bed fusion (LPBF) is a popular AM processing choice for metallic systems due to its relative speed, spatial resolution, and cost. In LPBF systems, a thin layer of powder (e.g., 20–100 μm) is melted and joined to a substrate by a small diameter (e.g., 25–100 μm) laser beam that traverses the area of the powder layer where metal is to be added to the part. This process is repeated, one layer at a time, until the desired shape results. The properties of a part built in this manner depend on the size distribution of flaws as a function of location and the final (post-build processed) microstructure. For optimal properties, the processing parameters need to be within a range of conditions that allows the laser to melt through the powder layer, and into the substrate far enough for flaw-free bonding of the added metal to the part. If the traversing laser has insufficient energy density for its velocity, then incomplete melting can result lack-of-fusion porosity. High energies can result in excessive melting that degrade part shape and finish, but even higher energies can vaporize metal pushing molten metal away from the laser producing spatter, keyholes, and melt pools filled with bubbles that become porosity on solidification. Obtaining high quality builds requires staying between these extremes so that essentially flaw-free bonds can be throughout the entire build [14, 15]. The conditions that define this "process window" may vary with any processing, build, or design variable, and could be significantly different from one part of a build to another. The velocities of the traverse laser in LPBF are fast enough to make closed-loop control through in-situ measurements challenging [16, 17]. Any solution to these challenges will either depend on, or will be greatly aided by, the development of accurate models for melt pool behavior and simulations of the LPBF process.

For laser powder bed fusion (LPBF), single autogenous laser tracks on smooth bare metal surfaces are simple experiments that can provide data on melt pool behavior that is free of variability due to the stochastic nature of the powder layer, and its properties, as well as substrate roughness and irregularities. The physics governing melt pool behavior for this experiment will be the same as that governing melt pool behavior during LPBF; but since the powder is absent, bulk alloy properties can be used for heat transfer, heat capacity, thermal expansion, and laser absorptivity [8, 18]. The solidified track remaining on the surface of the plate after the laser has passed is a physical record of the position of the air–liquid–solid interface at the edge of the melt pool as it solidifies behind the laser. Therefore, thorough characterization of the surface topography produced in these simple experiments will provide computer simulation groups with valuable data that can be used to guide development, or for the evaluation, comparison, and validation of models and simulations [19].

Experimental and Analytical Methods

Sample Preparation

Nickel alloy 625 (aka Inconel[1] 625, or IN625) was selected for the substrate because this nickel-based superalloy is (1) a single-phase solid-solution strengthened alloy (2) weldable (indicating the alloy responds well to non-equilibrium solidification) (3) relatively free of volatile alloying elements, (4) used in a large number of applications where AM parts could be economically competitive, and (5) a popular choice for AM part development due the reasons above, and the availability of powder. While this is a nominally single-phase solid-solution strengthened alloy, it should be kept in mind that there are a large number of precipitate phases that can form in this alloy depending on processing conditions [2, 5, 6, 20]. Therefore, modeling of the thermal history, solidification, phase nucleation, and growth could be very important contributions to the additive manufacturing of this alloy system.

Samples were cut from 3.2 mm thick plate of alloy 625 measuring approximately 24 mm by 25 mm. Initially, samples were prepared with four different surface finishes: (1) as-received (mill finish), (2) bead blasted (50 grit to 80 grit

glass beads followed by 120 grit alumina beads), (3) polished using standard metallurgical procedures to a randomly oriented, 320-grit finish using light pressure, and (4) polished using standard metallurgical procedures to a randomly oriented 320-grit finish using moderate pressure. Following preliminary examinations, the randomly oriented, 320-grit ground with moderate pressure finish was selected for the thorough analyses of this study.

Laser Tracks

Laser melt pool tracks were created in the samples using two different LPBF systems: (1) a commercial build machine (CBM), which was an EOS M270 modified at National Institute of Standards and Technology (NIST) by the addition of a high-speed short-wave infrared camera (SWIR) for measurement of melt pool lengths and cooling rates, and (2) the NIST Additive Manufacturing Metrology Testbed (AMMT). The samples produced in this equipment are designated as CBM and AMMT respectively. More details on these systems, and the in-situ measurements of the melt pools in these samples, can be found in other publications [11, 21–23].

Ten tracks, 16 mm long and spaced 0.5 mm apart were made in samples with each of the four surface finishes using three different power and speed settings in the CBM: (A) 150 W, 400 mm/s, (B) 195 W, 800 mm/s, and (C) 195 W, 1200 mm/s. After examination of these samples, a single surface finish (320-grit, moderate pressure, random orientation) was selected and an identical set of tracks were created in a sample with this surface finish in the AMMT. However, after the laser tracks were created, a recalibration of the AMMT found that the laser power calibration for the AMMT tracks was off by about 8%, and that the two systems used different definitions for diameter for the laser beam diameter setting. The actual values for the parameters used to create the tracks for these two systems are given in Table 1.

Confocal Scanning Laser Microscopy

The tracks were examined, recorded, and measured with a commercial confocal scanning laser microscope (CLSM) and the topography was quantified using commercial topographic analysis software designed for use with this instrument (Zeiss LSM 800 and ConfoMaps ST 7.4). This system is capable of both of wide-field and scanning laser (405 nm) illumination and the compiling of stitched and high depth of field images from tiled (field of view incrementally stepped in the x- or y-directions) and stacked (fixed field of view incrementally stepped in the z-direction) images. Bright field images of the entire length of all ten tracks in both samples were compiled from tiles taken with 5× and 10× objectives using wide-field illumination (with numerical apertures

Table 1 Parameters and conditions used in the creation of the laser melt pool tracks in the AMMT and CBM samples

Parameter	Description	AMMT	CBM
Laser spot size	D4σ[a]	170 μm	100 μm
	FWHM[b]	100 μm	59 μm
Laser scan	Length	16 mm	14 mm
Inert gas	Type	Argon	Nitrogen
	Flow	Laminar flow	Low flow
Oxygen level	Mol fraction	<0.08%	≈0.5%
Case A	Power	137.9 W	150 W
	Speed	400 mm/s	400 mm/s
	Quantity	3	3
Case B	Power	179.2 W	195 W
	Speed	800 mm/s	800 mm/s
	Quantity	3	3
Case C	Power	179.2 W	195 W
	Speed	1200 mm/s	1200 mm/s
	Quantity	4	4

[a]The 4 times the standard deviation diameter (D4σ) [24]

[b]The full width at half maximum (FWHM) diameter [24]

Table 2 The imaging conditions used for the detailed topographic analyses of the different track cases for the AMMT and CBM samples

Quantity	Value	Units
Laser wavelength	405	nm
Objective lens	20× apochromat 0.7 NA	
Pinhole	25	μm
Bit depth	8	bits
Image length (x)	16.16	mm
Image width (y)	638.90	μm
Image height (z)	Varied	
Δz step increment	0.180	μm
Pixel size (x, y)	0.624, 0.624	μm
Pixel depth	0.180	μm

(NA) of 0.13 and 0.25, respectively). For topographic analysis, stacked images were compiled for all ten tracks on both samples using the CLSM topographic analysis mode of this instrument and a 10×/0.4 NA objective lens. Then, one track was selected to represent each of the three cases in each sample type and the entire length (x), width (y), and height (z) was recorded using the scanning laser topography mode using imaging conditions given in Table 2.

The recorded image files were interpolated into surface data that were imported into the commercial topographic analysis software. Initially, the surface analysis software was used to examine the tracks as they were acquired, and slightly different analysis procedures may have been applied in different sequences with different settings. Therefore,

Table 3 Sequence of analysis steps used to evaluate the topography of the laser melt pool tracks using the commercial software package employed in this study

Step	Procedure	Settings/comments
1	Track surface data imported from LSM 800 to ConfoMaps	Data cutoff set to 4 and 256
2	Outliers removed	Default settings
3	Not measured points filled	Default settings
4	Image rotated to align the laser track and direction of laser motion with positive x-direction	$180 \pm 0.2°$
5	Extract area of interest: length (Δx) and width (Δy)	Ends: $\Delta x = 0.5$ mm; $\Delta y = 0.25$ mm Middle: $\Delta x = 8.0$ mm; $\Delta y = 0.25$ mm Others: Varied
6	Remove form: unaltered surface outside of melt pool tracks was fit to a 5th order polynomial which was then subtracted from surface data to make $z = 0$ at the initial surface	Initially, this step was 5th, but was moved to 6th when the tracks were reanalyzed
7	Analysis: surface roughness, longitudinal profiles (x-direction), transverse profiles (y-direction), or 3D maps	Areal parameters: ISO 25178 Linear parameters: ISO 4287 3D pseudo-color maps
8	Export results	File formats: txt; tiff; pdf

after all of the tracks had been acquired and analyzed, the analysis was repeated using exactly the same procedures, with the same settings, and in the same sequence for all 6 of the 20×/0.7 NA tracks used for detailed analysis. This sequence is outlined in Table 3. No significant differences resulted from this reanalysis of the data.

Initial Surface Finish

To quantify the original surface finish of the CBM and AMMT samples, CLSM surface topography data were determined for 3 areas, 0.250 mm wide and 8.00 mm long that were extracted from between the laser melt pool tracks of each sample. Areas free of spatter were selected and analyzed using the surface analysis software. These surface samples were oriented with the long dimension parallel to the direction of the laser scan and 8.00 mm long so that a line profile parallel to the direction of the laser scan would be the same length and contain the same number of points (12,823 points) as the laser melt pool centerline track profiles used to analyze the heights of the tracks. The software parameterizes surface areal data according to the ISO 25178 standard and linear profiles according to the ISO 4287 standard (using a 0.8 mm gaussian filter).

Melt Pool Track Analysis

Steady-state laser melt pool propagation behavior was characterized using surface data acquired with the CLSM using the settings in Table 2 for the entire length of a laser track representing each case and sample type and analyzed using the surface analysis software following the sequence outlined in Table 3. In step 4 of this analysis procedure (Table 3), the tracks were aligned with the positive x-direction parallel to

the direction of laser travel. In step 6 of this procedure, the location of the initial surface was estimated for each track by a curve fitting routine and subtracted from the height data for every (x, y) point. This results in a dataset representing the surface where the positive x-direction is the direction of laser travel and the z-value for every (x, y) point is a measure of the deviation above (+) or below (−) the estimated initial position of the surface at that point. With the positive x- and positive z-directions fixed, the positive y-direction is dictated by the conventions for a right-hand Cartesian coordinate system. Unlike the z-direction, where the zero point was always set at the estimated initial position of the surface, the zero point for both the x and y-directions are arbitrary, and were either set at the lower left corner of the sample, or at the estimated middle point of the track. Since the region of the track sampled to represent steady-state behavior needed to be well outside any region influenced by melt pool initiation at the start, or dissipation near the end, cumulative distribution functions (CDFs) for the track centerline heights (z) were created for different size samples centered about the mid-point of the track length. This examination found that when the samples included data from near either end of the tracks, deviations could be observed in the tails of the distributions. Therefore, to be well away from these deviations, the linear longitudinal and transverse profiles were taken from the middle 8.00 mm of the laser melt pool tracks.

The heights of the tracks were evaluated with a line profile down the centerline of the middle 8.00 mm of each track (12,823 points). For these profiles, y is constant, x is the independent variable, and z the dependent variable. To evaluate the stochastic nature of track height, the mean, standard deviation, minimum, maximum, and range were calculated from the height (z) data for each line profile. In addition, the centerline height data for each track were

converted into cumulative distributions and fit with the equation for a normal distribution.

To evaluate the transverse shape of the tracks, line profiles were taken perpendicular to the direction of laser travel at 1.00 mm intervals over the middle 8.00 mm of the tracks. This resulted in nine 0.25 mm long profiles consisting of 400 data points for each sample and case with y as the independent variable and z as the dependent variable (x being constant for each profile and an integer between 0 and 8). These profiles exhibited similar shapes with enough variation to indicate that this spacing was sufficient to consider these profiles to be independent random samples of the steady-state melt pool propagation behavior. The samples were aligned with the value of y set to zero at the track centerline and this enabled the averaging of the nine z-data points for each y-location to create an average profile to represent steady-state behavior for each sample and case.

Chevron Analysis

The tracks created in the surface of a metal behind the melt pool of a moving laser frequently contain V-shaped features known as chevrons. These chevrons are features that trail behind the melt pool with an apex that is located at, or near, the centerline of the track. The chevrons observed in this investigation were characterized in two ways: (1) density (or frequency) and (2) shape. The density of chevrons per mm of melt pool propagation was estimated by counting the number of chevron tips intersecting the track centerline in three 1.00 mm long 10× bright field micrographs of the track. The chevron shape was characterized by selecting seven representative chevrons for each sample and case from the bright field micrographs and then digitizing the traces of these chevrons over a distance of about ± 30 μm of the track centerlines. Since these bright field micrographs were taken normal to the original surface, these traced images are projections onto the x–y plane of features that may be inclined with respect to this plane. Within this distance of the track centerlines (± 30 μm), the chevrons have a nearly hyperbolic shape. The equation for a hyperbola with a transverse axis in the x-direction is

$$\frac{(x - d)^2}{a^2} - \frac{(y - e)^2}{b^2} = 1 \tag{1}$$

where d and e are the (x, y) coordinates of the center of the hyperbola, and $2a$ and $2b$ are the lengths of the transverse and conjugate axes of the hyperbola, respectively. To keep the notation consistent with that used for the track geometry, the chevron data were analyzed with the y-data as the independent variable and the x-data as the dependent variable. Solving the hyperbola equation above for x yields

$$x = \left(\frac{a}{b}\right)\sqrt{\left(b^2 + (y - e)^2\right)} + d. \tag{2}$$

Numerical data from the traced chevrons were fit to this equation with software that uses a Levenberg–Marquardt algorithm for least squares curve fitting [25]. The first derivative of this equation with respect to y is then

$$\frac{\mathrm{d}x}{\mathrm{d}y} = \frac{a(y - e)}{b\sqrt{b^2 + (y - e)^2}}. \tag{3}$$

According to this equation, the slope of the hyperbola, where it intersects its transverse axis at $y = e$, is zero, but when the distance (y) from transverse axis becomes large with respect to b, the slope approaches one of two constants depending on the direction taken from the transverse axis ($\pm a/b$). Therefore, the angle between the direction of laser travel (track centerline) and the asymptotes of a chevron ($\pm \alpha$) is

$$\alpha = \tan^{-1}\left(\frac{b}{a}\right) \tag{4}$$

where a and b are constants for the curves determined by the curve fitting software. The radius of curvature (ρ) of the of the chevron is related to the second derivative of Eq. (2) which is

$$\frac{\mathrm{d}^2 x}{\mathrm{d}y^2} = \frac{ab}{\left(b^2 + (y - e)^2\right)^{3/2}} \tag{5}$$

where a and b are again the constants determined for each individual chevron by curve fitting. Since at $y = e$, the first derivative is zero (0) and the second derivative is a/b^2, the radius of curvature at this point is

$$\rho = \left(\frac{\mathrm{d}^2 y}{\mathrm{d}x^2}\right)^{-1} = \left(\frac{b^2}{a}\right). \tag{6}$$

This value is used to represent the curvature of the chevron tip as estimated by the hyperbolic curve fit. The variability between chevrons for the same sample and case was large compared to the fitting uncertainties. Therefore, the variability of the population was estimated from the sample estimate of the standard deviation for the seven chevrons sampled for each sample type and case.

Fig. 1 Optical micrographs of the initial surface finishes examined in this study: **a** as-received, mill finish, **b** bead blasted, **c** 320 grit ground (light pressure), and **d** 320 grit ground (moderate pressure)
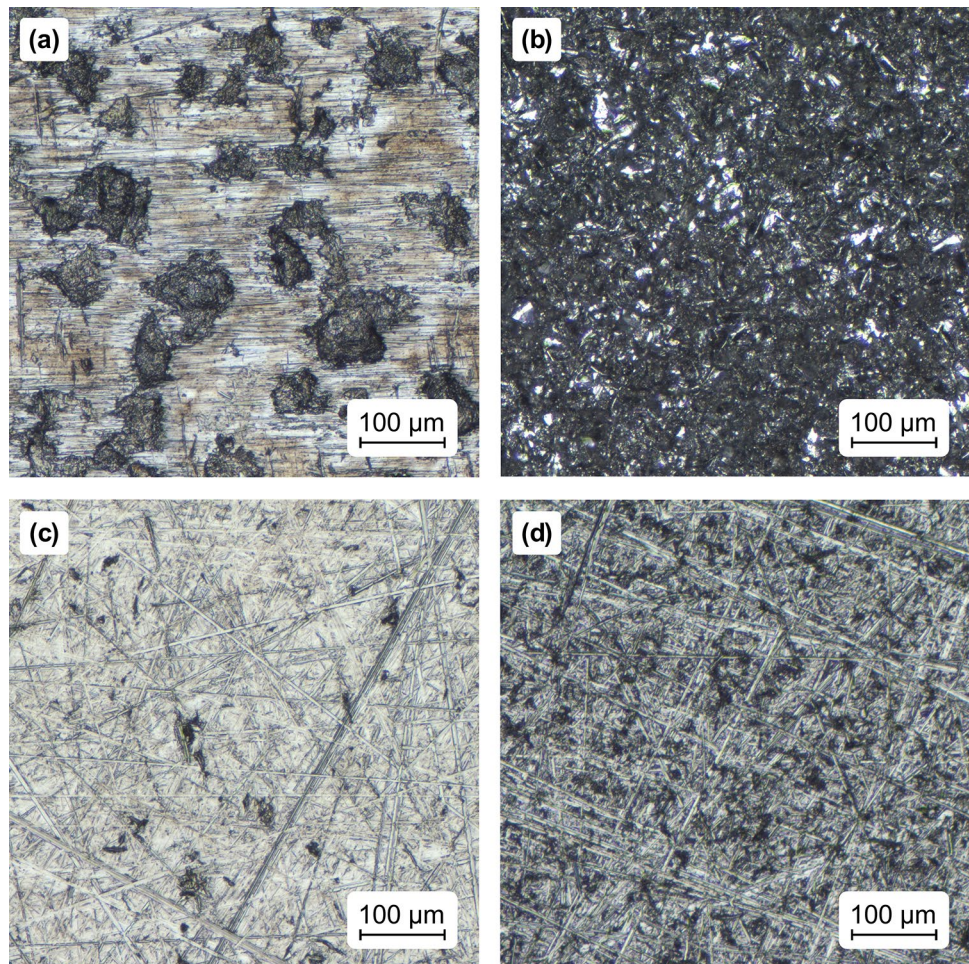

Results

Initial Surface Preparation

The four different surface finishes investigated at the start of this study are shown in the optical micrographs of Fig. 1: (a) the as-received, mill finish, (b) the bead-blasted finish, (c) the 320-grit, light pressure, random ground finish, and (d) the 320-grit, medium-pressure, random ground finish. This figure shows that the as-received mill finish had large dark areas in the surface, while the bead blasted finish contained smaller features, and the two ground finishes were primarily random arrays of scratches with smaller scratches observed for the lighter pressure case. Figure 2 shows 3D pseudo-color height maps of the same four surface finishes. This figure shows that the dark patches in the as-received sample were relatively deep depressions in the surface that frequently exceed 5 μm in depth and that the features in the bead-blasted finish corresponded to shorter wavelength oscillations in height with an amplitude that occasionally exceeded 5 μm. Figure 2c shows that the 320-grit ground with light pressure finish was smoother than that of the

moderate pressure case, shown in Fig. 2d, but that the lighter pressure failed to remove all of the depressions from the initial mill finish.

Figure 3 shows pseudo-color 3D height maps for 1.0 mm of steady-state laser track propagation produced at the same laser power and speed settings (Case B) for each of the four different surface finishes. In Fig. 3a, it can be seen that the centerline height of the laser melt pool track in the sample with the as-received mill finish sample exhibited long wavelength oscillations in height that are greater in amplitude than those shown for the 320-grit finishes (Fig. 3c, d). Closer examination of this image (including the 3D rotation of this image in the analysis software) revealed that these oscillations corresponded to locations where the melt pool intersected the depressions in the initial surface. Examination of Fig. 3b shows that the tracks in the bead-blasted surface contain discrete irregular features (bumps) of a size and shape similar to that of the media used for bead blasting this surface. Figure 3c, d show tracks created in the surfaces ground with 320 grit yielded melt pool tracks of similar character, though the surface outside the track is clearly rougher for the moderate pressure case.
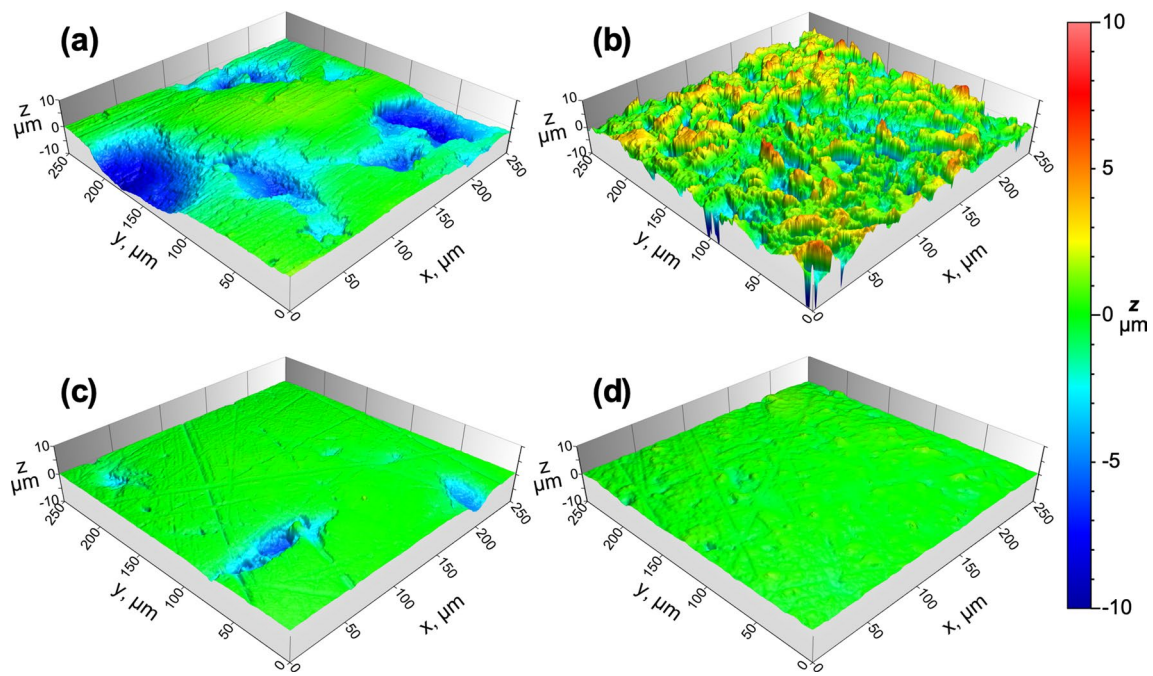
Fig. 2 Pseudo-color 3D height maps for the initial surface finishes examined in this study: **a** as-received, mill finish, **b** bead blasted, **c** 320 grit ground (light pressure), and **d** 320 grit ground (moderate pressure)
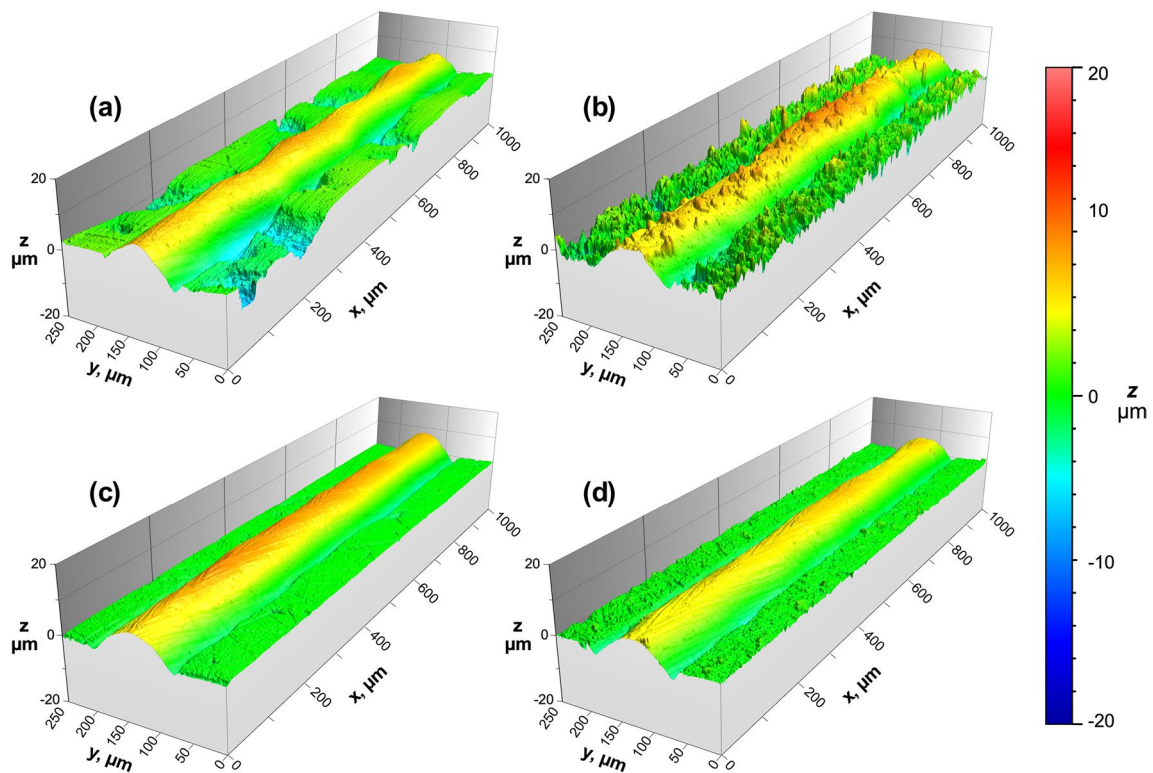
Fig. 3 Pseudo-color 3D height maps of a Case B track created in IN625 samples with different initial surface finishes: **a** as-received, mill finish, **b** bead blasted, **c** 320 grit ground (light pressure), and **d** 320 grit ground (moderate pressure)
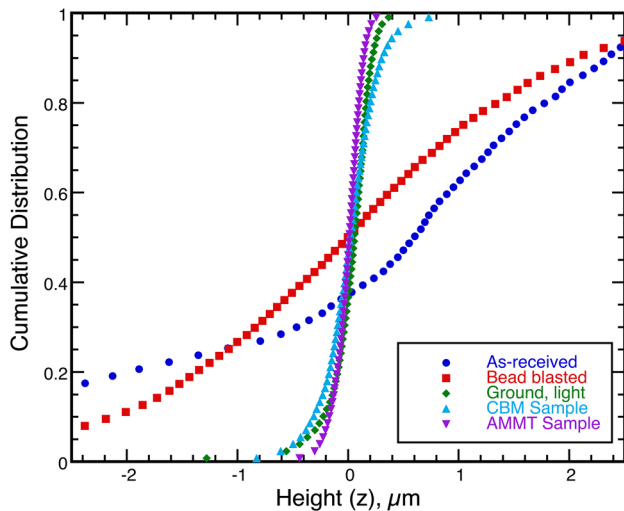
Fig. 4 Cumulative distributions of the height measurements from 8.00 mm long linear profiles of the initial surface finishes examined taken parallel to the direction of laser travel

Figure 4 shows cumulative surface height (z) distributions for 8.00 mm long linear profiles taken from the unaltered surface between laser tracks in the CBM samples for the four different initial surface finishes, and in the AMMT sample. This figure shows that range of the height distribution for the three 320-grit finishes was significantly less than that of the other finishes. The areal and profile surface roughness parameters determined by the analysis software for three different regions of each of the samples are given in Table 4 [26, 27].
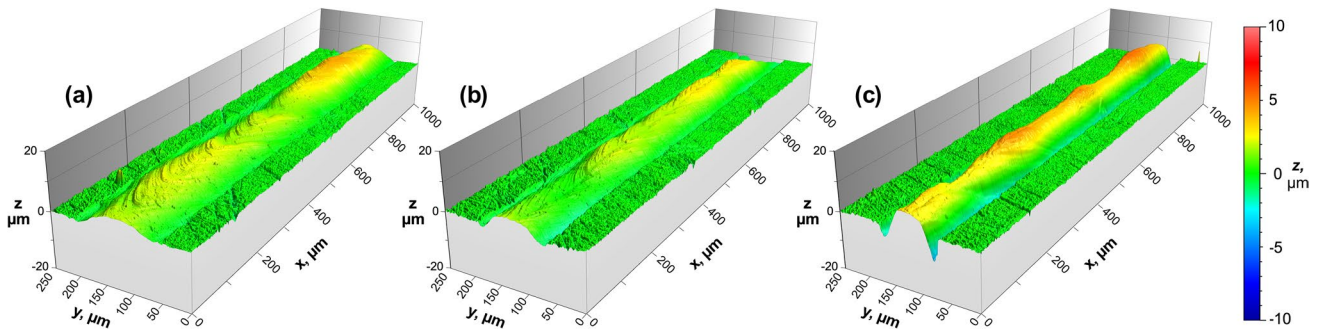
Steady-State Melt Pool Track Topography

Figure 5 shows 3D pseudo-color height maps for 1.00 mm of melt pool propagation in the middle of the laser melt pool tracks for the three case settings on the AMMT sample; and in Fig. 6, for the three different case settings on the CBM sample. It should be noted that while the maps in each figure have the same height range, the height range for the three maps in Fig. 5 is half of that used for Fig. 6 (20 μm vs. 40 μm). As shown in these figures, a typical track consisted of a peak at, or near, the track centerline with troughs of varying depth near the edges of the tracks.
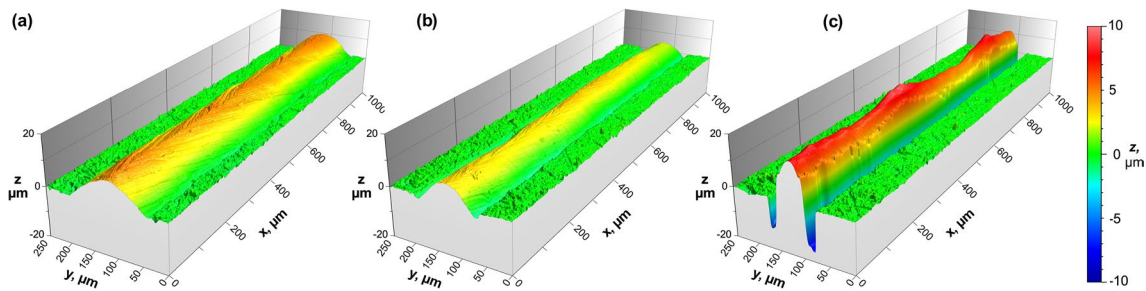
The mean and standard deviation values calculated from the track centerline height data for each sample and case are given in Table 5. Figure 7 shows cumulative distributions (CDFs) of the same data with the distributions for the initial surface condition of the samples included. When the CDFs were fit to a normal distribution, the resulting correlation coefficients (r) were all above 0.995 and the lines, shown in Fig. 7, are those for the curve fits. The parameters determined by this curve fitting are included in Table 5 for comparison to the calculated values of the same parameters.

The mean transverse profile for each sample and case was determined by averaging the height data for the same y-location with respect to the track centerline for the nine transverse samples of that sample and case. The resulting transverse mean height profiles are shown in Fig. 8. The error bars in this figure represent the standard deviation calculated for the nine measurements at the location where the error bar is shown. In addition, the mean,

Table 4 Areal and profile surface roughness parameters determined for the different initial surface finishes investigated

Sample	Area	S_q^a (μm)	S_z^a (μm)	S_a^a (μm)	R_q^b (μm)	R_z^b (μm)	R_a^b (μm)
As-received mill finish	A	2.210	20.322	1.707	1.987	8.547	1.523
	B	2.218	17.168	1.724	1.569	6.936	1.202
	C	2.333	17.670	1.786	1.785	7.412	1.382
Bead blasted	A	1.850	26.847	1.441	1.624	9.460	1.260
	B	1.850	22.383	1.447	1.541	9.222	1.195
	C	1.843	18.827	1.447	1.543	9.329	1.214
Ground light pressure	A	0.348	12.086	0.201	0.195	1.209	0.132
	B	0.351	7.605	0.192	0.188	1.180	0.134
	C	0.330	7.494	0.188	0.235	1.543	0.148
CBM sample	A	0.316	8.783	0.228	0.260	1.981	0.191
	B	0.338	10.704	0.245	0.244	1.955	0.177
	C	0.320	7.365	0.231	0.249	1.967	0.183
AMMT sample	A	0.169	7.339	0.123	0.121	0.899	0.091
	B	0.160	4.229	0.116	0.124	0.997	0.091
	C	0.160	6.754	0.114	0.116	0.835	0.086

[a] Areal parameters defined in ISO 25178 [26]

[b] Linear profile parameters defined in ISO 4287 (0.8 mm gaussian filter) [27]

Fig. 5 Pseudo-color 3D height maps for 1.00 mm of melt pool propagation for tracks created in the AMMT: **a** Case A track, **b** Case B track, and **c** Case C track

Fig. 6 Pseudo-color 3D height maps for 1.00 mm of melt pool propagation for tracks created in the CBM: **a** Case A track, **b** Case B track, and **c** Case C track

Table 5 Laser melt pool track centerline (CL) height distribution parameters calculated from the data and from fitting the data to a normal distribution

Sample	Track case	Mean CL Height (z) (μm)	SD (z) (μm)	Max (z) (μm)	Min (z) (μm)	Range (μm)
Calculated distribution parameters						
AMMT	A	2.113	0.951	4.992	− 1.112	6.104
AMMT	B	1.657	1.221	4.818	− 2.835	7.653
AMMT	C	3.394	1.456	6.451	− 0.716	7.166
CBM	A	9.993	1.197	12.740	7.027	5.712
CBM	B	6.776	0.806	8.934	4.717	4.216
CBM	C	13.280	2.175	19.682	8.793	10.889

| Sample	Track case	Mean (z) (μm)	Uncertainty (mean) (μm)	SD (μm)	Uncertainty (SD) (μm)	Correlation coef., R
Distribution parameters determined by curve fitting						
AMMT	A	2.085	0.0003	0.869	0.001	0.999
AMMT	B	1.713	0.0005	1.116	0.001	0.999
AMMT	C	3.530	0.001	1.369	0.002	0.997
CBM	A	10.077	0.001	1.229	0.002	0.996
CBM	B	6.772	0.0002	0.837	0.0004	0.999
CBM	C	13.201	0.001	2.036	0.001	0.999

SD standard deviation

standard deviation, and range for the maximum heights of the nine transverse profiles for each sample and case are given in Table 6 along with the same quantities for the minimum height.
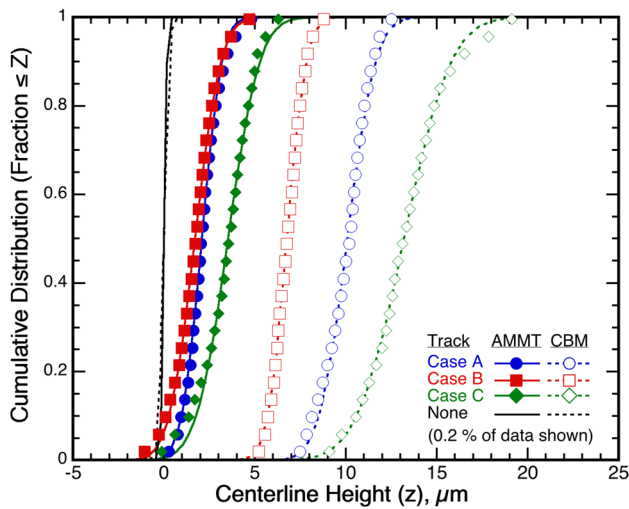
Fig. 7 Cumulative distributions of the measured heights over 8 mm of melt pool track for each case in each build machine and the initial starting surface profiles for each sample
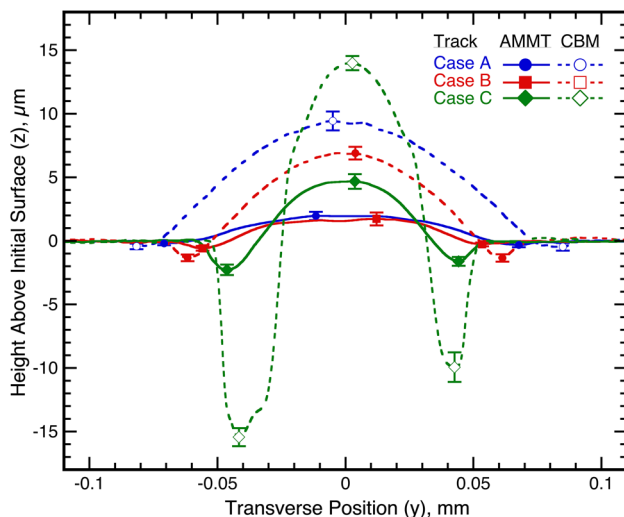
Fig. 8 Mean height at different y-positions for nine transverse profiles for each case and build machine examined. The transverse profiles were spaced 1 mm apart ($\Delta x = 1.0$ mm) over the middle 8.0 mm of each track. Each curve contains about 400 points with each point being the mean for the 9 measurements taken at that y-location. The standard deviation for select points is shown with error bars in the figure

Figure 9 shows bright field micrographs of a portion of the tracks created by steady-state melt pool propagation for the three different cases in each of the two types of samples. Chevrons can be seen in five of these micrographs, but there is no evidence of a feature of this type in the CBM Case C micrograph (Fig. 9d). The mean densities and standard deviations determined for the chevrons are given in Table 7. The seven chevrons selected, traced, and digitized to represent

each sample type and case are shown in Fig. 10. The correlation coefficients (r^2) for the hyperbolic fits to these chevrons ranged from 0.966 to 0.999. The mean and standard deviation of the parameters determined by the hyperbolic curve fitting of the seven samples for each sample type and case are given in Table 7.

Track Start and Finish Topography

The start ends of the tracks are shown in Fig. 11 for the AMMT sample and in Fig. 12 for the CBM sample. As with the steady-state propagation figures, a greater height range was required to show the ends of the CBM tracks (50 μm vs. 20 μm). As these figures indicate, the highest point for each track was the peak at the start end. Figure 13 shows the longitudinal profiles (x–z plane) through the middle of the start-end of the six tracks and Fig. 14 shows transverse profiles (z–y plane) through the highest point in the six tracks.

The finish ends of the tracks are shown in Figs. 15 and 16 for the AMMT and CBM samples, respectively. As with the start ends, a much greater height range was required to display the ends of the CBM tracks (60 μm vs. 20 μm). Also, while the maps for the AMMT tracks capture what appears to be the entire depression at the track end, the depressions at the ends of the CBM tracks exceed the 0.5 mm length of these figures. As these figures indicate, the lowest point for each track was found in the finish end. Figures 17 and 18 are the longitudinal (x–z plane) and transverse (z–y plane) profiles for the track finish ends. In these figures, there are horizontal dashed lines to indicate the estimated position of the original surface. In these figures, the longitudinal profiles are down the centerline of the tracks and the transverse profiles are through the lowest point.

Discussion

Initial Surface Preparation

The initial, as-received, surface finish of the alloy plate contains depressions as shown in Figs. 1 and 2. When a propagating melt pool intersects one of the depressions, it appears that liquid metal flows into the depression increasing the width of the melt pool and decreasing its height. This also results in an initial surface finish where the mean and the median are significantly different as shown in Fig. 4. This could make estimation of the location of the initial surface by surface analysis software troublesome. Therefore, it was determined that some form of surface preparation was required. While one might be able to reduce the range of roughness in a bead-blasted surface from that observed here, the retention of some of the blasting media in the surface

Table 6 Data for the maximum and minimum heights determined over 9 transverse profiles from the middle 8.00 mm of laser melt pool track

Sample	Case	Mean	SD	Max	Min	Range
Maximum height (z) (μm)						
AMMT	A	2.130	0.619	2.882	0.965	1.917
AMMT	B	1.949	0.846	3.352	0.559	2.793
AMMT	C	4.802	1.097	6.584	3.552	3.031
CBM	A	9.618	1.497	11.674	7.499	4.174
CBM	B	7.000	0.978	8.604	5.637	2.967
CBM	C	14.044	1.086	16.058	12.501	3.557
Minimum height (μm)						
AMMT	A	− 0.593	0.264	− 0.115	− 0.904	0.789
AMMT	B	− 0.836	0.304	− 0.351	− 1.136	0.785
AMMT	C	− 2.660	0.680	− 1.423	− 3.570	2.147
CBM	A	− 1.090	0.545	− 0.439	− 1.859	1.421
CBM	B	− 1.703	0.593	− 1.166	− 2.870	1.704
CBM	C	− 15.735	1.558	− 14.330	− 18.254	3.924
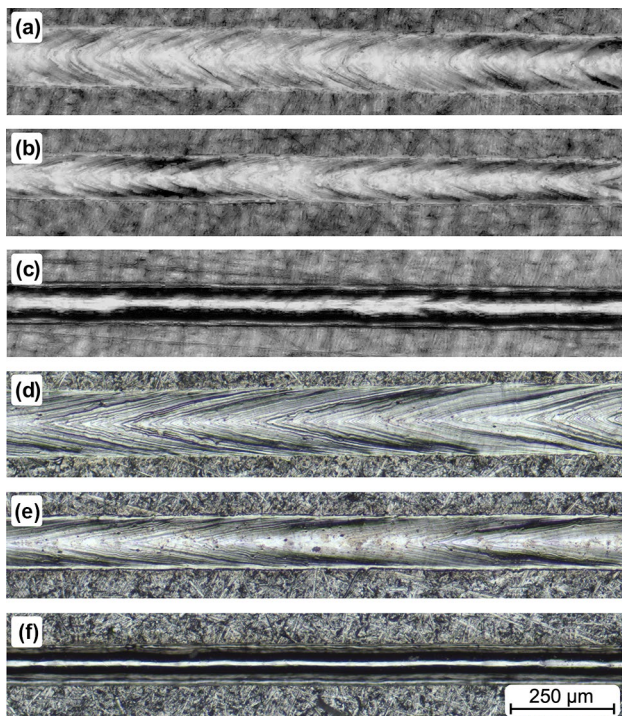
Fig. 9 Bright field micrographs showing the chevrons: **a** AMMT Case A track, **b** AMMT Case B track, **c** AMMT Case C track, **d** CBM Case A track, **e** CBM Case B track, and **f** CBM Case C track

that might interfere with measurements makes any variation of this approach unacceptable. Therefore, grinding the surface with 320-grit was the surface finish selected for the samples used for the thorough topographic analyses. The abrasion direction used was varied in a random fashion to avoid any bias that could result if the scratches all had the same orientation. Based on partial retention of the as-received depressions shown in Fig. 2, when the applied

pressure was too light, greater pressures and times were used for these samples.

Steady-State Melt Pool Track Topography

The results show that the smaller laser beam size used to generate the melt pool tracks in the CBM sample resulted in tracks with higher peaks near the centerline, and deeper troughs at the edges. Assuming that no metal is added, or lost, during steady-state melt pool propagation, and that the solidified tracks are free of porosity, then the volume of metal above the initial surface should be equal to that below it during steady-state propagation. Detailed analysis of this assumption is highly dependent on the estimation of the location of the initial surface, metal vaporization, and porosity that goes beyond the scope of the present work. However, this implies that the tracks with the higher peaks should have lower troughs which are consistent with the tracks shown in Figs. 5 and 6 and the transverse cross sections shown in Fig. 8.

Examination of Figs. 8 and 9 shows that while the tracks in the CBM sample were made with a smaller diameter beam, the melt pools produced in Case A and Case B were slightly wider than those produced for the same Cases in the AMMT sample. An answer is implied by the comparison of the Case B and Case C track for the CBM sample. These two tracks were created using the same laser energy and beam diameter, but different laser speeds (800 mm/s vs. 1200 mm/s). The higher peaks and deeper troughs of the Case C track resulted in a narrower track width and chevrons were not observed for this case. This transition should be an interesting challenge for modeling. Clearly, understanding how to create a smooth surface without generating deep, crack-like groves, or embedded flaws, would be a worthy objective for the modeling community to address.

Table 7 Results for the analysis of the chevrons created during steady-state laser melt pool propagation

Quantity	Track case	AMMT		CBM		Units
		Mean	SD	Mean	SD	
Frequency ($n=3$)	A	84.7	17.5	72	7.5	#/mm
	B	39.7	10.1	42.7	4.0	
	C	39.3	1.5	0.0	0.0	
Transverse axis constant (a)	A	43.2	13.9	26.3	21.5	μm
	B	49.2	10.3	21.2	14.9	
	C	301.6	524.0	–	–	
Conjugate axis constant (b)	A	18.8	3.5	5.58	3.53	μm
	B	13.9	2.4	3.63	2.36	
	C	26.8	29.6	–	–	
Chevron asymptote slope (b/a)	A	0.450	0.061	0.227	0.031	m/m
	B	0.285	0.024	0.183	0.022	
	C	0.188	0.088	–	–	
Angle to transverse axis (α)	A	24.15°	2.90°	12.77°	1.71	degrees
	B	15.92°	1.28°	10.35°	1.20	
	C	10.56°	4.88°	–	–	
Curvature (b^2/a)	A	8.28	0.64	1.21	0.62	μm
	B	3.96	0.69	0.63	0.38	
	C	3.16	1.48	–	–	

The sample size (n) is seven except for the frequency analysis where n was 3. The sample standard deviation estimate, that uses ($n-1$), was used to calculate standard deviations. Chevrons were not observed in the CBM Case C tracks
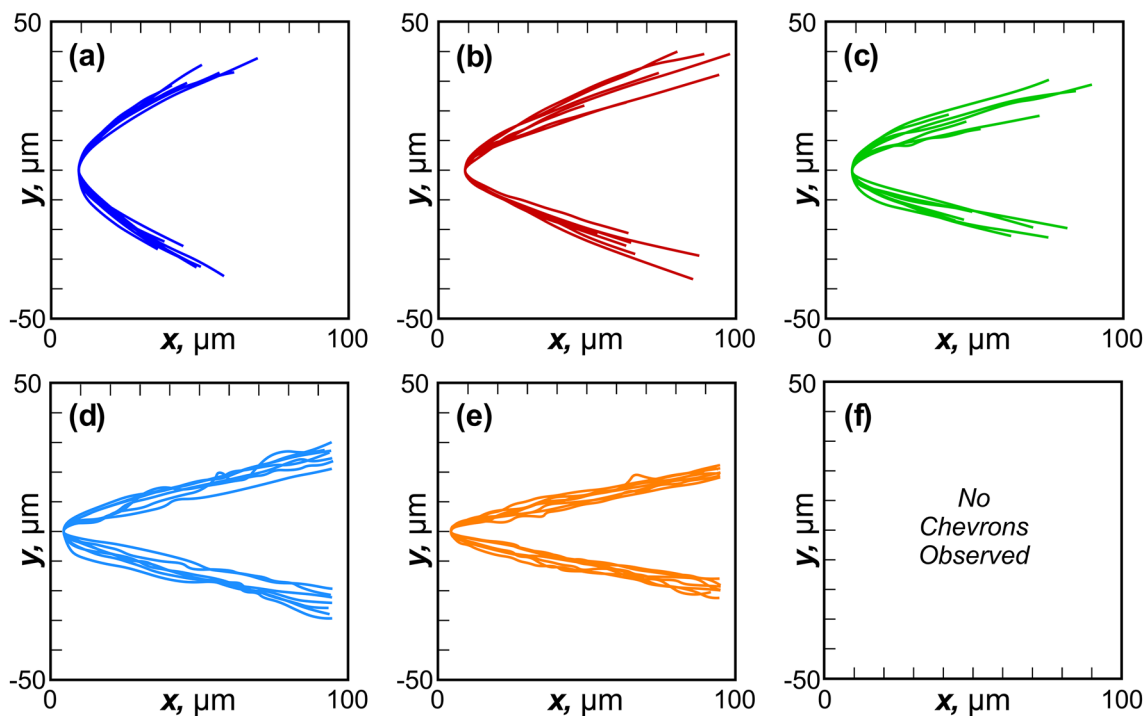
Fig. 10 Seven overlaid chevron tip profiles traced from optical micrographs: **a** AMMT Case A track, **b** AMMT Case B track, **c** AMMT Case C track, **d** CBM Case A track, **e** CBM Case B track, and **f** CBM Case C track
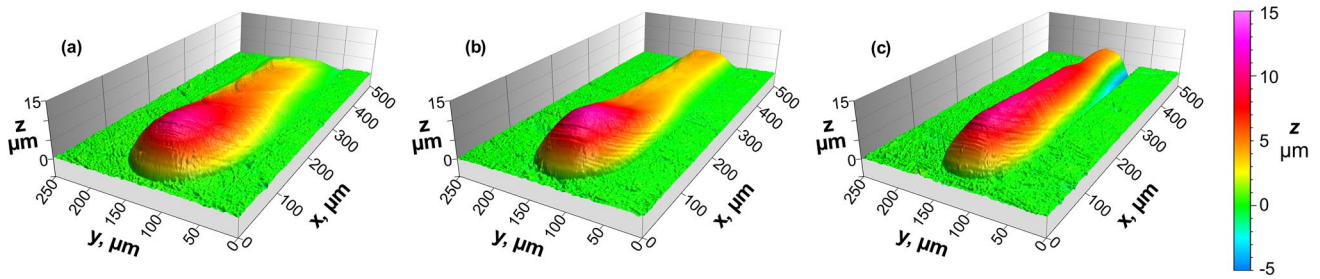
Fig. 11 Pseudo-color 3D height maps of the start end of tracks created in the AMMT: **a** Case A track, **b** Case B track, **c** Case C track
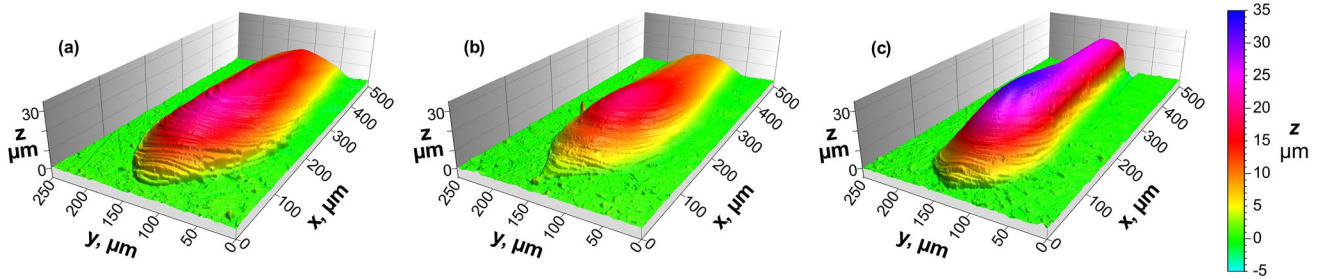

Fig. 12 Pseudo-color 3D height maps of the start end of tracks created in the CBM: **a** Case A track, **b** Case B track, **c** Case C track
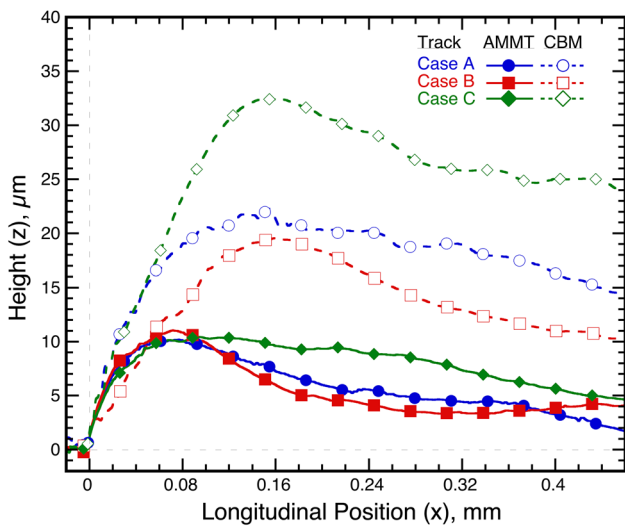

Fig. 13 Longitudinal centerline profiles of the start-ends tracks created in both the AMMT and CBM (only 2% of data points are shown)
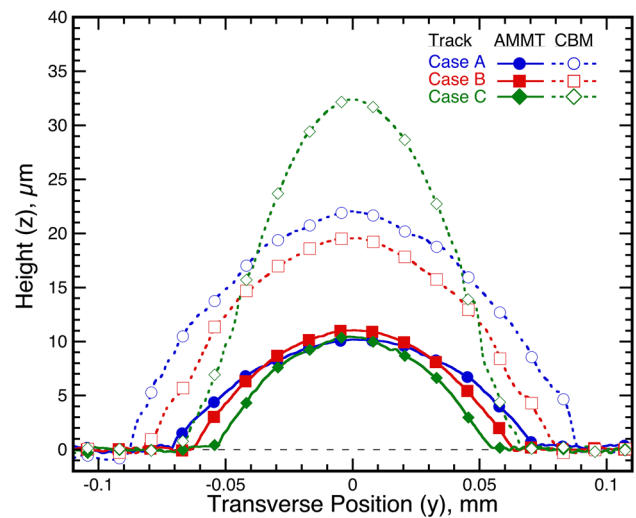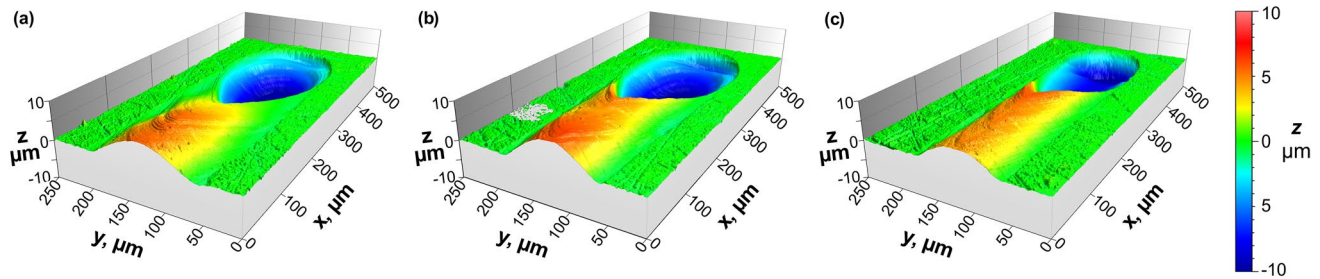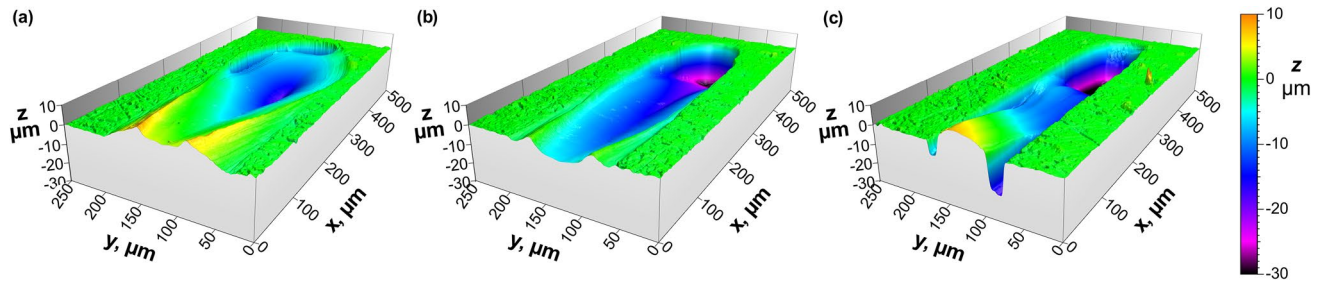
Fig. 14 Transverse line profiles through the highest point of the start ends for tracks created in both the AMMT and CBM (only 5% of data points are shown)

Presumably, the chevrons are records of the edge of the melt pool at different points in time. In situ, high spatial resolution, fixed-view imaging at 10,000 frames per second using in-line laser illumination confirms this assumption that chevrons indicate the edge of the melt pool [11]. As such, the chevrons must start at the leading edge of the melt pool and taper from the circular shape of the laser at its widest, to an apex near the centerline where solidification is the slowest and occurs last. Therefore, the apexes of the chevrons are near the location where the tracks are the highest, and open up to the edges of the tracks, where the heights of the tracks are below the original surface. Therefore, the chevrons are inclined with respect to the initial surface indicating that the melt pool is also inclined. This can be seen in the 3D pseudo-color maps of the finish ends shown in Figs. 15 and 16. This makes distinction of chevrons, and estimation of their density, easier at the centerline.

Fig. 15 Pseudo-color 3D height maps of the finish end of tracks created in the AMMT: **a** Case A track, **b** Case B track, **c** Case C track

Fig. 16 Pseudo-color 3D height maps of the finish end of tracks created in the CBM: **a** Case A track, **b** Case B track, **c** Case C track
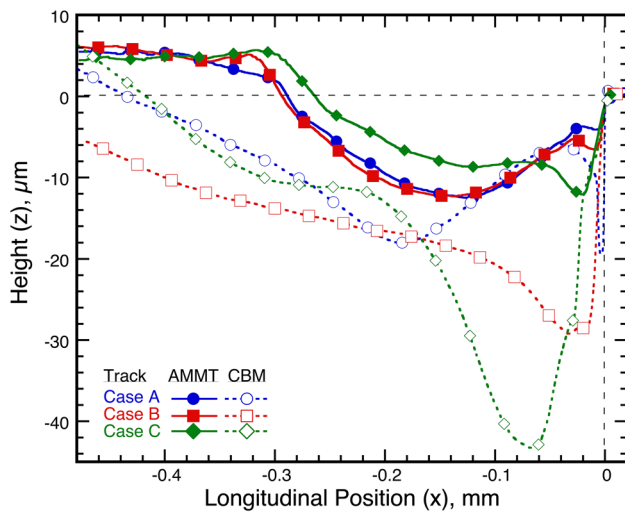
Fig. 17 Longitudinal centerline profiles of the finish ends of tracks created in both the AMMT and CBM (only 2% of data points are shown)
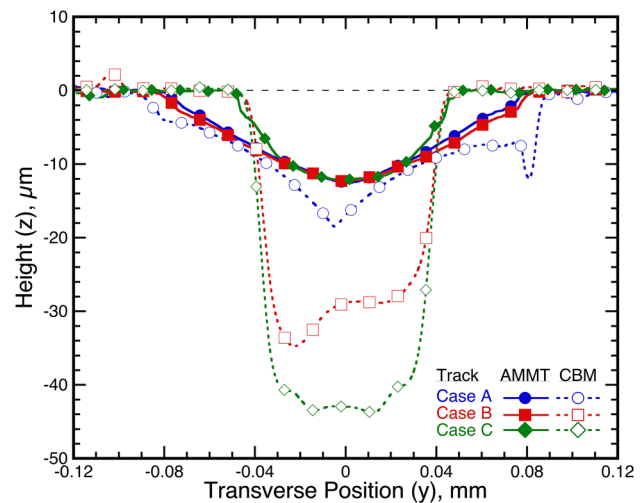
Fig. 18 Transverse line profiles through the lowest point of the finish ends of tracks created in the AMMT and CBM (only 5% of data points are shown)

Track Start and Finish Topography

The highest and lowest point of each track occurred at the starting and finishing laser positions, respectively. This, of course, is due to the physics of the laser interactions with the melting surface, including depression of the molten metal under the laser from the recoil effect, and its accumulation in the trailing edge of the melt pool as it solidifies. While the topography of these features is not indicative of steady-state propagation, they are indicative of the fundamental nature of these interactions, and the perturbations that occur at the start and finish. Examination of the start ends shown Figs. 11 and 12 shows that the oscillations in the melt–solid interface at the edge of the melt pool that produce the chevrons start immediately as the melt pool forms and starts moving; but initially, these melt pool line marks are more circular presumably due to the power distribution of the laser beam.

These lines start transitioning to the classic chevron shape by the time that the maximum height is reached.

Figure 13 and Fig. 14 show the longitudinal and transverse profiles through the highest point in the six tracks. These show that the highest point occurred at the almost the same location for all three cases in each sample, but different locations for the different samples. In Fig. 13, it can be seen that the maximum height is reached in the first 80 μm for all three cases in the AMMT sample, but is not reached until about 160 μm for all three cases in the CBM sample where the laser beam diameter was smaller. Presumably, this is due to the higher concentration of energy creating a deeper melt pools in the CBM sample and a greater "backwash" of molten metal behind the melt pool. This also implies that a longer time and distance of propagation was required for steady-state propagation to get established in this sample.

The depressions at the finish ends of the tracks are shown in Figs. 15 and 16. If one assumes that the solidification rate in the melt pool when the laser is switched off is high compared to the rate that liquid metal can reflow back into the depression, then the shape of this depression will be indicative of the shape of the melt pool depression. Keeping this assumption in mind, the longitudinal and transverse profiles of Figs. 17 and 18 indicate that the melt pool was depressed significantly deeper for the CBM sample than the AMMT sample. This is consistent with the steady-state melt-pool cross sections described elsewhere [11]. Starting at the end-point of the track, and moving in the negative x-direction, all six tracks have a steep decline with a positive slope where melting of the substrate was just getting started when the laser was shut-off. This decline is followed by a local minimum, after which the slope changes sign becoming negative. Then, all six tracks reach a point where the sign of the slope changes back to positive going to a second local minimum before reverting back to negative and increasing toward the steady-state centerline height. While not obvious in all six cases, this occurrence of the second local minimum was confirmed in all six cases by expanding the z-scale. For the Type C tracks of both samples, and the CBM Type A track, the minima closer to the track end was the deeper, while the reverse was true for the other tracks. For the CBM Type B, the second minima was close to the first one (≈ 10 μm) while for the CBM Type C track the second minimum was about 250 μm from the first. It appears that this morphology is related to the fundamental behavior of melt pool under the laser and competition between the recoil pressure pushing molten metal out from under the laser while gravity pulls it back. This conclusion is reached even though: (1) the slope of these curves frequently exceeded that which an objective lens with a numerical aperture of 0.7 can capture, (2) curve fitting was required to estimate these positions, and (3) some reflow of metal has to have occurred before solidification fixed these positions, due to the similarity of these profiles to

the ultrafast in-situ x-ray images of laser melting and simulations of other investigators [28–30].

The transverse profiles of Fig. 18 show that the maximum depths of the finish-end depressions in the AMMT sample were very similar, but very different in the CBM sample. The wider laser beam used for the AMMT tracks appears to be responsible for this observation; but since the transverse profiles were taken at the location of the maximum depth of the finish-end depression, their position with respect to the center of the laser at shut-off may vary considerably. For example, Fig. 17 shows the location of the maximum depth is much closer to the tip of the finish end for the AMMT Case C track than it is for the other two AMMT tracks. Also, that the CBM Case A track was profiled the furthest from the finish-end tip. Therefore, it is concluded that additional detailed analysis of the finish ends would be required to support any modeling effort addressing the morphology of these features.

Summary and Conclusions

The objective of this study was to create autogenous laser melt pool tracks in IN625 samples using two different types of LPBF machines with similar laser power and speed settings; and then, to thoroughly quantify the morphology of the tracks created in such a manner that the data can be used for the development and benchmarking of models, and simulations, of the LBPF process. This has been accomplished. This study found that the morphology created by steady-state melt pool propagation tends to vary stochastically about a mean position or shape. When a characteristic of this shape was quantified, it was found that it could be represented by a normal distribution with distribution parameters that depend on the build conditions used to create the tracks (e.g., Fig. 7 and Table 5). The start and finish ends of the tracks were indicative of the laser-alloy interactions, but at this time it is unclear how much back-filling, flow, and solidification has altered their appearance, and how to best interpret these features. In addition to providing benchmark data for modeling of melt pool behavior, the examination of single autogenous laser tracks, and overlapping autogenous tracks, could be a relatively simple, rapid, and inexpensive means of evaluating the amenability of an alloy to the high thermal gradients, solidification rates, and stresses inherent in additive manufacturing.

References

1. Lass EA, Stoudt MR, Williams ME (2019) Additively manufactured nitrogen-atomized 17-4 PH stainless steel with mechanical properties comparable to wrought. Metall Mater Trans A 50:1619–1624

2. Lindwall G, Campbell CE, Lass EA, Zhang F, Stoudt MR, Allen AJ, Levine LE (2018) Simulation of TTT curves for additively manufactured Inconel 625. Metall Mater Trans A 50:457–467

3. Lass EA, Stoudt MR, Katz MB, Williams ME (2018) Precipitation and dissolution of δ and γ″ during heat treatment of a laser powder-bed fusion produced Ni-based superalloy. Scr Mater 154(9):83–86

4. Zhang F, Levine LE, Allen AJ, Stoudt MR, Lindwall G, Lass EA, Williams ME, Idell Y, Campbell CE (2018) Effect of heat treatment on the microstructural evolution of a nickel-based superalloy additive-manufactured by laser powder bed fusion. Acta Mater 152:200–214

5. Stoudt MR, Lass EA, Ng DS, Williams ME, Zhang F, Campbell CE, Lindwall G, Levine LE (2018) The influence of annealing temperature and time on the formation of δ-phase in additively-manufactured Inconel 625. Metall Mater Trans A 49(7):3028–3037

6. Lass EA, Stoudt MR, Williams ME, Katz MB, Levine LE, Phan TQ, Gnaeupel-Herold TH, Ng DS (2017) Formation of the Ni_3Nb δ-phase in stress-relieved Inconel 625 produced via laser powder-bed fusion additive manufacturing. Metall Mater Trans A 48(11):5547–5558

7. Zhang F, Levine LE, Allen AJ, Campbell CE, Lass EA, Cheruvathur S, Stoudt MR, Williams ME, Idell Y (2017) Homogenization kinetics of a nickel-based superalloy produced by powder bed fusion laser sintering. Scr Mater 131:98–102

8. Keller T, Lindwall G, Ghosh S, Ma L, Lane BM, Zhang F, Kattner UR, Lass EA, Heigel JC, Idell Y, Williams ME, Allen AJ, Guyer JE, Levine LE (2017) Application of finite element, phase-field, and CALPHAD-based methods to additive manufacturing of Ni-based superalloys. Acta Mater 139:244–253

9. Stoudt MR, Ricker RE, Lass EA, Levine LE (2017) Influence of postbuild microstructure on the electrochemical behavior of additively manufactured 17-4 PH stainless steel. JOM 69(3):506–515

10. Cheruvathur S, Lass EA, Campbell CE (2016) Additive manufacturing of 17-4 PH stainless steel: post-processing heat treatment to achieve uniform reproducible microstructure. JOM 68(3):930–942

11. Lane BM, Heigel JC, Zhirnov I, Khromchenko VB, Ricker R, Phan T, Stoudt M, Mekhontsev SN, Levine LE (2019) Measurements of melt pool geometry and cooling rates of individual laser traces on IN625 bare plates. Integr Mater Manuf Innov (topical collection on the AM-Bench 2018 test series)

12. Stoudt M, Williams ME, Claggett S, Heigel JC, Levine LE (2019) Location-specific microstructure within 3D AM builds of 15-5 and IN625 AM-bench artifacts. Integr Mater Manuf Innov (topical collection on the AM-bench 2018 test series)

13. Levine L, Lane B, Heigel J, Migler K, Stoudt M, Phan T, Ricker R, Strantza M, Hill M, Zhang F, Seppala J, Garboczi E, Bain E, Cole D, Allen A, Fox J, Campbell C (2019) Outcomes and conclusions from the 2018 AM-bench measurements, challenge problems, modeling submissions, and conference. Integr Mater Manuf Innov (topical collection on the AM-Bench 2018 test series)

14. Clymer DR, Cagan J, Beuth J (2017) Power–velocity process design charts for powder bed additive manufacturing. J Mech Des 139(10):100907

15. Bidare P, Bitharas I, Ward RM, Attallah MM, Moore AJ (2018) Fluid and particle dynamics in laser powder bed fusion. Acta Mater 142:107–120

16. Grasso M, Colosimo BM (2017) Process defects and in-situ monitoring methods in metal powder bed fusion: a review. Meas Sci Technol 28(4):044005

17. Everton SK, Hirsch M, Stravroulakis P, Leach RK, Clare AT (2016) Review of in-situ process monitoring and in-situ metrology for metal additive manufacturing. Mater Des 95:431–445

18. Ma L, Fong J, Lane B, Moylan S, Filliben JJ, Hecker A, Levine L (2015) Using design of experiments in finite element modeling to identify critical variables for laser powder bed fusion. In: Proceedings of the 26th annual international solid freeform fabrication symposium: an additive manufacturing conference. The University of Texas at Austin

19. Ghosh S, Ma L, Levine LE, Ricker RE, Stoudt MR, Heigel JC, Guyer JE (2018) Single-track melt-pool measurements and microstructures in Inconel 625. JOM 70(6):1011–1016

20. Suave LM, Cormier J, Villechaise P, Soula A, Hervier Z, Bertheau D, Laigo J (2014) Microstructural evolutions during thermal aging of alloy 625: impact of temperature and forming process. Metall Mater Trans A 45(7):2963–2982

21. Lane B, Mekhontsev B, Grantham S, Vlasea ML, Whiting J, Yeung H, Fox J, Zarobila C, Neira J, McGlauflin M, Hanssen L, Moylan S, Donmez A, Rice J (2016) Design, developments, and results from the NIST additive manufacturing metrology testbed (AMMT). In: International solid freeform fabrication symposium—an additive manufacturing conference, 2016, pp 1145–1160

22. Lane B, Moylan S, Whitenton E, Ma L (2016) Thermographic measurements of the commercial laser powder bed fusion process at NIST. Rapid Prototyp J 22(5):778–787

23. Heigel J, Lane B, Phan T, Brown D, Strantza M, Levine L (2019) Sample design and in-situ characterization of cooling rate and melt pool length during 3D AM builds of 15-5 and IN625 AM-Bench artifacts. Integr Mater Manuf Innov (topical collection on the AM-bench 2018 test series)

24. Wikipedia contributors, Beam Diameter (2019). https://en.wikipedia.org/w/index.php?title=Beam_diameter&oldid=889049881. Accessed 23 July 2019

25. Bates DM, Watts DG (1988) Nonlinear regression analysis and its applications. Wiley, New York

26. ISO (2017) ISO 25178: geometric product specifications (GPS)—surface texture: areal. In: T. 213 (ed.) International Organization for Standardization (ISO)

27. ISO (1997) ISO 4287: geometrical product specifications (GPS)—surface texture: profile method—terms, definitions and surface texture parameters. In: T. 213 (ed.) International Organization for Standardization (ISO)

28. Parab ND, Zhao C, Cunningham R, Escano LI, Fezzaa K, Everhart W, Rollett AD, Chen L, Sun T (2018) Ultrafast X-ray imaging of laser-metal additive manufacturing processes. J Synchrotron Radiat 25(Pt 5):1467–1477

29. Cunningham R, Zhao C, Parab N, Kantzos C, Pauza J, Fezzaa K, Sun T, Rollett AD (2019) Keyhole threshold and morphology in laser melting revealed by ultrahigh-speed x-ray imaging. Science 363(6429):849–852

30. Martin AA, Calta NP, Khairallah SA, Wang J, Depond PJ, Fong AY, Thampy V, Guss GM, Kiss AM, Stone KH, Tassone CJ, Nelson Weker J, Toney MF, van Buuren T, Matthews MJ (2019) Dynamics of pore formation during laser powder bed fusion additive manufacturing. Nat Commun 10(1):1987